International Journal for Modern Trends in Science and Technology
Volume 12, Issue 08, pages 51-65.
ISSN: 2455-3778 online
Available online at: http://www.ijmtst.com/vol12issue06.html
DOI: https://doi.org/10.5281/zenodo.22120037

Enhanced Transient Stability and Grid Power Quality of a Solar PV Based DC Microgrid Using Hybrid Energy Storage under Pulsed Loads

T. Tharun Raj | C Praveen | M. Harish

Department of Electrical & Electronics Engineering, Sri Venkatesa Perumal College of Engineering and Technology, Puttur, Andhra Pradesh, India.

To Cite this Article
T. Tharun Raj, C Praveen & M. Harish (2026). Enhanced Transient Stability and Grid Power Quality of a Solar PV Based DC Microgrid Using Hybrid Energy Storage under Pulsed Loads. International Journal for Modern Trends in Science and Technology, 12(08), 51-65. https://doi.org/10.5281/zenodo.22120037

Article Info
Received: 29 June 2026; Revised: 09 July 2026; Accepted: 12 July 2026.

KEYWORDS

DC microgrid, hybrid energy storage system, battery energy storage system, supercapacitor, photovoltaic system, pulsed load, voltage source converter, transient stability, power quality, total harmonic distortion.

ABSTRACT

This paper presents a grid-connected DC microgrid incorporating a hybrid energy storage system (HESS) comprising a battery energy storage system (BESS) and a supercapacitor (SC) for enhanced transient stability and power quality under pulsed-load conditions. The proposed system integrates a photovoltaic (PV) source, BESS, SC, DC loads, and a voltage source converter (VSC) for controlled power exchange with the utility grid. The BESS supplies the low-frequency and sustained power component, while the SC compensates for high-frequency power fluctuations and rapid pulsed-load transients. A bidirectional converter is employed to control the power exchange of the HESS with the DC bus, while the grid-side VSC regulates the DC-bus voltage and transfers excess power to the utility grid through an LC filter. The proposed control strategy reduces DC-bus voltage fluctuations, limits battery current transients, and improves the dynamic response of the microgrid during sudden load and renewable-power variations. In addition, the SC mitigates rapid disturbances reaching the grid-side converter, thereby improving the quality of the grid current and reducing total harmonic distortion (THD). The effectiveness of the proposed HESS-based grid-connected DC microgrid is evaluated under constant and pulsed-load operating conditions. Simulation results demonstrate improved DC-bus voltage regulation, reduced transient deviations, lower battery current stress, and enhanced grid-current quality compared with a conventional BESS-based DC microgrid. The proposed configuration provides a reliable and resilient solution for renewable-integrated grid-connected DC microgrids subjected to dynamic and pulsed power demands.

I. Introduction

The increasing integration of renewable energy sources (RESs), distributed energy resources, and power electronic converters has significantly promoted the development of microgrid technology for modern power systems. Microgrids provide an effective platform for integrating distributed generation, energy storage systems, and local loads while improving energy efficiency, reliability, flexibility, and controllability [1]. The hierarchical control concept for microgrids has further enabled coordinated operation of distributed energy resources and power converters under different operating conditions [2]. With the increasing penetration of renewable generation, microgrids are becoming an important component of future decentralized power systems [3], [4]. Among different microgrid configurations, dc microgrids have attracted considerable research interest because several renewable energy sources, energy storage devices, electric vehicles, and electronic loads are inherently dc in nature. The use of a dc distribution structure can reduce unnecessary power conversion stages and associated losses, thereby improving the overall conversion efficiency of the system [5]. In addition, different dc microgrid architectures and applications have been investigated for residential, commercial, transportation, data-center, and industrial applications [6]. The advantages and challenges associated with dc distribution systems have also been extensively analyzed, particularly with respect to voltage regulation, power sharing, protection, and converter interaction [7]. Compared with conventional ac microgrids, dc microgrids can provide a direct interface for several renewable and storage technologies, making them attractive for renewable-integrated power systems [8]. Solar photovoltaic (PV) generation is one of the most promising renewable energy sources for dc microgrid applications because of its modularity, scalability, low operating requirements, and environmental benefits. Accurate PV modeling is essential for predicting the electrical characteristics of the PV array under different irradiance and temperature conditions [9]. Maximum power point tracking (MPPT) techniques are generally employed to extract the maximum available power from the PV system under changing environmental conditions [10]. However, the intermittent nature of solar irradiation causes continuous variations in PV power generation. When these variations occur simultaneously with changes in load demand, a power imbalance can develop between generation and consumption. Such an imbalance can directly influence the dc-bus voltage and consequently affect the stability and dynamic performance of the microgrid. The dc-bus voltage is therefore a critical parameter in a dc microgrid because it represents the instantaneous balance between generated power, load power, and stored energy. Several voltage regulation and power-sharing methods have been proposed to maintain stable dc-bus operation under varying operating conditions [11]. Improved droop-based control techniques have also been developed to achieve accurate current sharing and dc-bus voltage restoration in dc microgrids [12]. However, rapid load variations and intermittent renewable generation can produce transient voltage deviations that require an energy storage system with sufficiently fast power-response capability. Consequently, energy storage has become an essential component of renewable-energy-based dc microgrids. Different ESS technologies have been investigated for renewable-energy applications based on their energy density, power density, response time, efficiency, lifetime, and cost [13]. Conventional battery energy storage systems (BESSs) are widely used because of their relatively high energy density and capability to provide sustained power over extended periods [14]. Batteries are therefore suitable for compensating slow variations in renewable generation and maintaining the energy balance of the microgrid. However, the dynamic response of batteries is comparatively slower than that of high-power storage technologies. Frequent high-current charging and discharging can also increase electrical and thermal stress and accelerate battery degradation [15]. Supercapacitors (SCs) offer complementary characteristics to batteries. They provide high power density, rapid charge-discharge capability, and high cycle life, making them suitable for short-duration and high-power transient compensation [16]. However, the comparatively low energy density of SCs limits their suitability for supplying sustained power over long periods [17]. Therefore, the combination of a BESS and SC in a hybrid energy storage system (HESS) provides an attractive solution by combining high-energy and high-power storage characteristics. The battery can supply the average and low-frequency power component, whereas the SC can provide the high-frequency and transient power component [18]. Battery-SC HESSs have been investigated extensively for renewable-energy and transportation applications. Their complementary characteristics allow the battery to operate under relatively smoother current conditions while the SC handles rapid power variations [19]. HESSs have also been investigated for high-power applications where rapid changes in power demand cannot be efficiently handled by batteries alone [20]. The reduction of battery current fluctuations is particularly important because excessive transient currents can increase battery losses and reduce its useful operating lifetime. A suitable hybridization strategy can therefore improve both the dynamic performance of the microgrid and the utilization of the individual storage devices. The advantages of HESS become more significant when the dc microgrid supplies pulsed loads. Unlike conventional loads, pulsed loads can produce sudden increases and decreases in power demand within a short time interval. Such rapid power variations can result in significant dc-bus voltage sag or overshoot if adequate transient power is not available. A battery-only storage system must respond directly to these power pulses, resulting in large battery-current variations. Battery-supercapacitor hybridization has been shown to reduce the transient power requirement imposed on the battery under pulsed-load conditions [21]. Consequently, the SC can absorb or supply rapid power changes while the BESS provides the required sustained power. The effectiveness of HESS operation depends strongly on the adopted power management strategy. Several control methods have been proposed for separating the power demand between the battery and SC, including frequency-based, rule-based, fuzzy, optimization-based, and predictive control approaches. A coordinated power management strategy can improve dc-bus voltage regulation while reducing the high-frequency current component supplied by the battery [22]. Advanced control techniques have also been investigated to improve power sharing between storage devices and enhance the dynamic response of dc microgrids [23]. Optimization-based HESS power management has further demonstrated the potential to coordinate battery and SC operation according to load requirements and storage constraints [24]. In a grid-connected dc microgrid, the voltage source converter (VSC) provides the interface between the dc bus and the utility grid. The VSC can regulate the dc-bus voltage, control active-power exchange, and transfer surplus renewable power to the utility grid. However, sudden changes in dc-side power can influence the operating conditions of the grid-side converter and may introduce disturbances into the grid current. Appropriate coordination between the HESS and grid-side VSC is therefore required to maintain stable dc-bus operation and satisfactory grid power quality. Dynamic power management and coordinated control of HESS-based dc microgrids have demonstrated improvements in voltage regulation and system response [25]. In addition, advanced energy-management techniques can improve the utilization of hybrid storage devices under rapidly varying operating conditions [26]. The interaction between PV generation, HESS, pulsed loads, and power electronic converters makes transient stability and power quality important performance requirements for grid-connected dc microgrids. During a sudden load pulse, the SC should rapidly compensate for the transient power so that the dc-bus voltage remains close to its reference value. The BESS should preferably provide the low-frequency and sustained component of the load power, thereby limiting rapid battery-current variations. Studies on HESS-based dc microgrids have demonstrated that appropriate power management can improve the dynamic performance and reduce battery stress [27]. In addition, advanced control methods have been applied to HESS-based systems to improve voltage regulation under pulsing-load conditions [28]. Although several studies have investigated battery-SC HESSs, existing research has primarily focused on energy management, battery lifetime improvement, standalone operation, or renewable-power smoothing. Comparatively less attention has been given to the simultaneous evaluation of dc-bus transient stability and grid-side power quality in a grid-connected PV-based dc microgrid subjected to pulsed loads. In particular, the coordinated operation of the BESS, SC, bidirectional converter, dc bus, and grid-side VSC during rapid load transitions remains an important research area. Recent investigations of HESS control under pulsing-load conditions indicate that fast storage response can significantly improve voltage regulation and system stability [29]. However, further work is required to simultaneously address transient voltage deviation, battery-current stress, and grid-current quality in a renewable-integrated grid-connected dc microgrid [30]. To address these limitations, this paper proposes a grid-connected solar PV-based dc microgrid incorporating a battery-SC HESS for enhanced transient stability and grid power quality under pulsed-load conditions. The proposed system consists of a PV source, BESS, SC, bidirectional HESS converter, dc loads, grid-side VSC, utility grid, and LC filter. The BESS is responsible for supplying the low-frequency and sustained power component, whereas the SC provides rapid compensation for high-frequency power fluctuations and sudden pulsed-load transients. The bidirectional converter regulates the power exchange between the HESS and dc bus, while the grid-side VSC maintains the dc-bus voltage and controls power exchange with the utility grid. During a sudden increase in load demand, the SC rapidly supplies the required transient power, thereby reducing the current stress imposed on the BESS. When the pulsed load is removed, the SC absorbs the transient excess power and assists in limiting dc-bus voltage overshoot. Consequently, the proposed HESS improves dc-bus voltage regulation, reduces battery-current fluctuations, and enhances the transient response of the microgrid. Furthermore, the reduction in rapid disturbances transferred to the grid-side VSC, together with the LC filter, contributes to improved grid-current quality and reduced total harmonic distortion (THD).

The main contributions of the proposed work are summarized as follows:

- A grid-connected solar PV-based DC microgrid is developed by integrating a PV source, BESS, supercapacitor, bidirectional HESS converter, DC loads, grid-side VSC, utility grid, and LC filter.
- A battery-supercapacitor HESS configuration is employed to exploit the complementary characteristics of the two storage technologies. The BESS supplies the low-frequency and sustained power component, while the SC compensates for high-frequency power fluctuations and rapid load transients.
- An effective power-sharing strategy is implemented between the BESS and SC to ensure appropriate utilization of the two storage devices during normal and pulsed-load operating conditions.
- DC-bus voltage stability is enhanced during sudden load changes by using the fast-response capability of the SC to compensate for the transient power imbalance.
- Battery current stress is reduced by preventing the BESS from responding directly to high-frequency pulsed-load variations, thereby improving battery operating conditions and potentially reducing degradation.
- Transient performance under pulsed loads is improved by enabling the SC to rapidly supply or absorb short-duration power variations, resulting in reduced voltage sag, voltage overshoot, and improved recovery time.
- Grid-side power quality is improved through coordinated operation of the HESS and grid-side VSC, while the LC filter attenuates high-frequency switching components in the grid current.

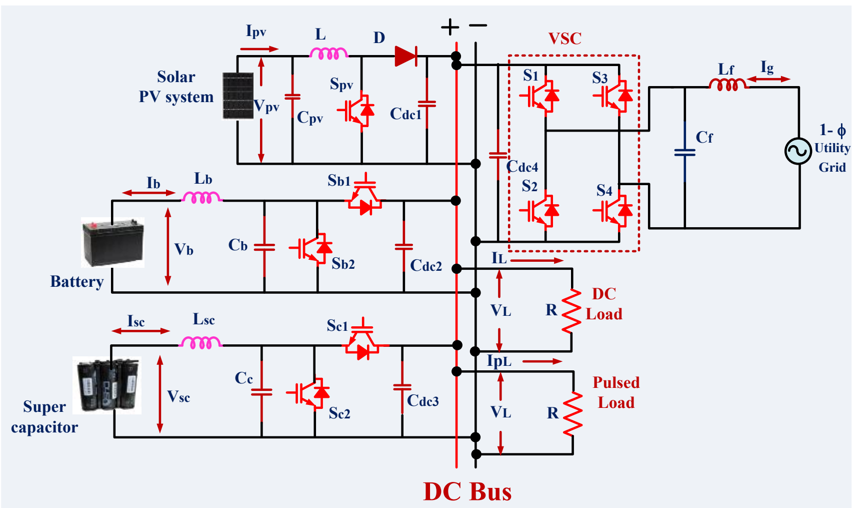

Fig. 1. Configuration of the Grid-Connected Solar PV-Based DC Microgrid with Hybrid Energy Storage System and Pulsed Loads.

II. Modeling of the PV System

The solar PV subsystem consists of a PV array, DC-link capacitor, DC–DC boost converter, MPPT controller, and PI-based voltage control. The PV array converts solar irradiance into electrical DC power. The variable PV output is connected to the boost converter, which increases the PV voltage to the required DC-bus voltage of the proposed DC microgrid. The boost converter consists of an inductor L, switching device Spv, diode D, and DC-link capacitor Cdcas shown in Fig.2. The P&O MPPT controller continuously determines the optimum operating point of the PV array. The measured PV voltage is compared with the MPPT reference voltage, and the error is processed by the PI controller to generate the PWM signal for the boost-converter switch.

The photovoltaic (PV) array is the primary renewable energy source in the proposed EV charging system. It converts solar irradiance into electrical energy through the photovoltaic effect. The electrical behavior of the PV module is represented by the single-diode equivalent circuit shown in Fig. 3, which consists of a photocurrent source Iph, a diode D, a series resistance Rs, and a shunt resistance Rp. The series resistance represents the internal conduction losses, whereas the shunt resistance accounts for the leakage current within the PV cell.

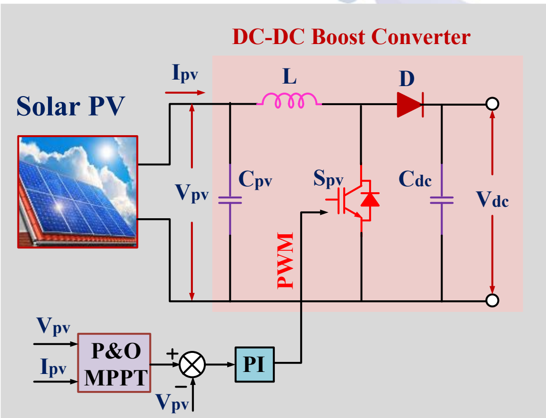

Fig. 2 Solar PV System with P&O MPPT

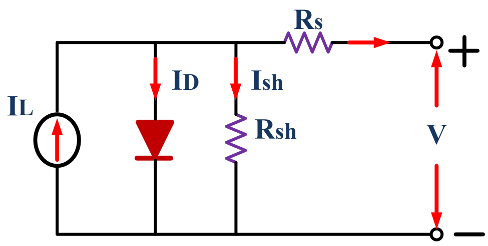

Fig. 3. Single-diode equivalent circuit of the photovoltaic (PV) module.

The output current of the PV module is obtained by applying Kirchhoff's current law to the equivalent circuit and is expressed as

$$I_{PV} = I_{Ph} - I_D - I_{sh} \quad (1)$$

Where I_{PV} is the output current, I_D is the diode current, and I_{sh} is the shunt leakage current.

According to the Shockley diode equation, the diode current is given by

$$I_D = I_o\left[\exp\left(\frac{q(V_{pv}+I_{pv}R_s)}{AkT}\right) - 1\right] \quad (2)$$

Where I_o is the reverse saturation current, q is the electron charge (1.602×10−19C), A is the diode ideality factor, k is Boltzmann's constant (1.381×10−23J/K), and T is the cell temperature in Kelvin.

The shunt current flowing through the parallel resistance is expressed as

$$I_{sh} = \frac{V_{PV}+I_{PV}R_S}{R_P} \quad (3)$$

Substituting (2) and (3) into (1), the complete current–voltage characteristic of the PV module becomes

$$I_{PV} = I_{Ph} - I_0\left[\exp\left(\frac{q(V_{pv}+I_{pv}R_s)}{AkT}\right) - 1\right] - \frac{V_{PV}+I_{PV}R_S}{R_P} \quad (4)$$

The photocurrent generated by the PV module depends on the solar irradiance and operating temperature and is calculated as

$$I_{Ph} = [I_{sc} + K_i(T - T_{ref})]\frac{G}{G_{ref}} \quad (5)$$

Where I_{sc} is the short-circuit current, K_i is the temperature coefficient of current, G is the incident solar irradiance, and G_{ref} is the reference irradiance under standard test conditions.

The output power of the PV array is obtained as

$$P_{PV} = V_{PV}I_{PV} \quad (6)$$

III. Perturb and Observe (P&O) MPPT Algorithm

To maximize the energy extracted from the PV array, a Perturb and Observe (P&O) MPPT algorithm is employed as shown in Fig.4. The controller periodically measures the PV voltage and current and computes the output power

$$P(k) = V(k)I(k) \quad (7)$$

The variations in power and voltage are calculated as

$$\Delta P = P(k) - P(k-1) \quad (8)$$

$$\Delta V = V(k) - V(k-1) \quad (9)$$

The operating voltage is updated according to the following decision rules:

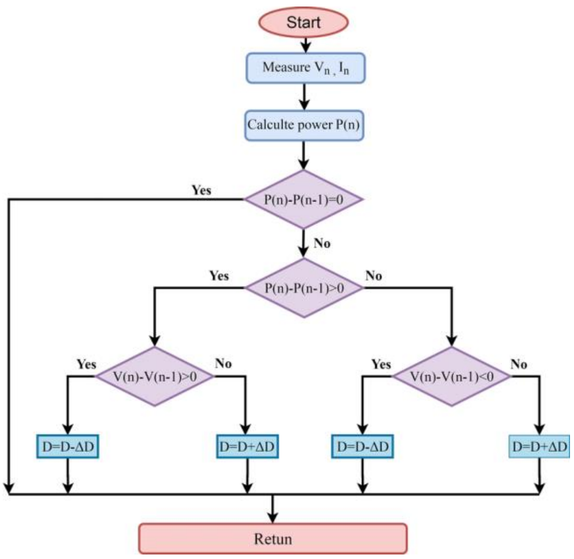

Fig.4 flow chart of P&O MPPT algorithm

- If

$\Delta P > 0, \Delta V > 0$ (10)

increase the reference voltage.

- If

$\Delta P > 0, \Delta V < 0$ (11)

decrease the reference voltage.

- If

$\Delta P < 0, \Delta V > 0$ (12)

decrease the reference voltage.

- If

$\Delta P < 0, \Delta V < 0$ (13)

increase the reference voltage.

The updated reference voltage is expressed as

$$V_{ref}(k-1) = V_{ref}(k) \pm \Delta V \quad (14)$$

The voltage error is

$$e(k) = V_{ref} - V_{pv} \quad (15)$$

The PI controller generates the control signal

$$u(k) = K_p e(k) + K_i \int e(k)\, dt \quad (16)$$

The PWM duty ratio is then obtained as

$$D = \frac{u(k)}{V_C} \quad (17)$$

Where V_C is the carrier signal amplitude.

By continuously updating the duty ratio, the P&O algorithm forces the PV array to operate at the maximum power point despite variations in solar irradiance and temperature. The regulated output of the boost converter maintains a stable DC bus voltage while maximizing renewable energy utilization.

IV. BESS-Based Bidirectional DC–DC Buck–Boost Converter

The BESS is interfaced with the common DC bus through a bidirectional DC–DC buck–boost converter, as shown in Fig. 5. The converter consists of the battery source, input capacitor Cb, inductor Lb, complementary semiconductor switches Sb1 and Sb2, and the DC-bus interface. The input capacitor suppresses high-frequency voltage ripple, whereas the inductor limits the battery-current ripple and facilitates controlled bidirectional power transfer. The converter is operated using a PI-based battery-current control scheme, in which the reference battery current Ibess∗ is compared with the measured battery current Ibess. The resulting error is processed by the PI controller, and its output is converted into PWM switching signals for Sb1 and Sb2.

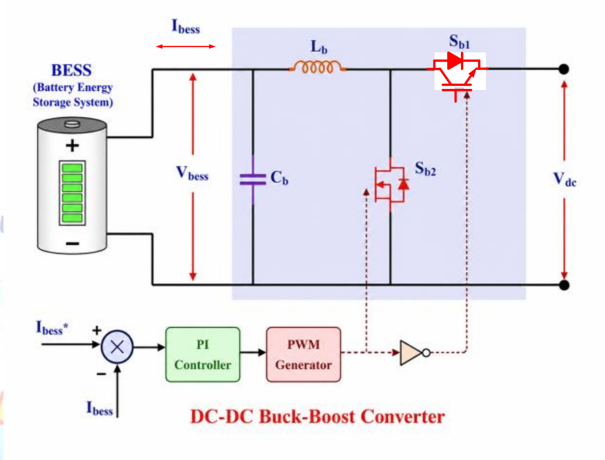

Fig. 5. Bidirectional DC-DC buck-boost converter for battery energy storage system.

The battery-current error is expressed as

$$e_b(t) = I^*_{bess}(t) - I_{bess}(t) \quad (18)$$

The PI controller generates the control signal according to

$$u_b(t) = K_p e_b(t) + K_i \int e_b(t)\, dt \quad (19)$$

where K_p and K_i are the proportional and integral gains, respectively. The corresponding transfer function is

$$G_{PI}(s) = K_P + \frac{K_i}{s} \quad (20)$$

During BESS discharging, the battery supplies power to the DC bus when the PV power is insufficient to satisfy the load demand. The converter operates in boost mode, and the power flow is

$$P_{bess} = V_{bess} I_{bess} \quad (21)$$

For an ideal boost operation, the relationship between the battery voltage and DC-bus voltage is given by

$$V_{dc} = \frac{V_{bess}}{1-D} \quad (22)$$

where D is the converter duty ratio. Thus, the required duty ratio is

$$D = 1 - \frac{V_{bess}}{V_{dc}} \quad (23)$$

During the ON state of the lower switch Sb2, the inductor stores energy from the battery, and its current increases according to

$$V_{Lb} = L_b \frac{dI_{Lb}}{dt} \quad (24)$$

When Sb2 is turned OFF, the stored inductor energy is transferred toward the DC bus through the upper switching path Sb1. Consequently, the battery provides the required transient and sustained power to maintain the DC-bus power balance.

During BESS charging, the direction of power flow is reversed. Excess PV power available on the DC bus is transferred through the converter to charge the battery. The converter operates in buck mode, and the ideal voltage relationship is

$$V_{bess} = DV_{dc} \quad (25)$$

The corresponding duty ratio is

$$D = \frac{V_{bess}}{V_{dc}} \quad (26)$$

The battery-side capacitor Cb is used to reduce voltage fluctuations and high-frequency switching components. Its voltage-current relationship is

$$I_{C_b} = C_b \frac{dV_{bess}}{dt} \quad (27)$$

Similarly, the inductor current ripple is approximately given by

$$\Delta I_{L_b} = \frac{V_{bess}D}{L_b^{fs}} \quad (28)$$

where fs is the converter switching frequency. A suitable value of Lb therefore ensures smooth battery-current operation and limits excessive current ripple.

V. Supercapacitor-Based Bidirectional DC–DC Buck–Boost Converter

The supercapacitor (SC) is interfaced with the common DC bus through a bidirectional DC–DC buck–boost converter, as shown in Fig. 6. The converter consists of the supercapacitor, input capacitor Csc, inductor Lsc, complementary switches Ssc1 and Ssc2, and the DC-bus interface. The supercapacitor is primarily employed to compensate for the high-frequency and short-duration power variations produced by pulsed loads. The capacitor Csc suppresses high-frequency voltage ripple, while Lsc limits the supercapacitor current ripple and provides smooth bidirectional power transfer.

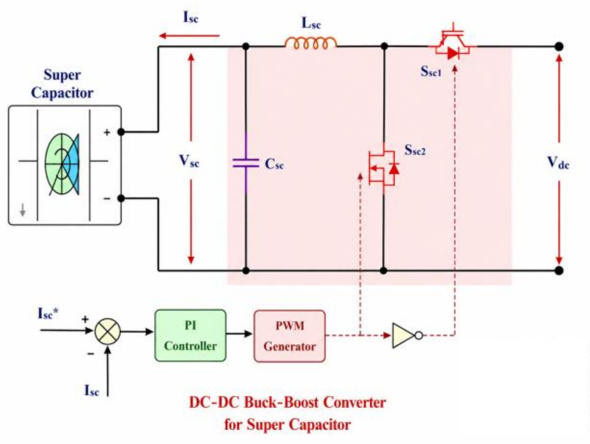

Fig. 6. Bidirectional DC-DC buck-boost converter for supercapacitor energy storage system.

The SC current error is obtained by comparing the reference current Isc∗ with the measured current Isc, given by

$$e_{sc}(t) = I_{sc}^{*}(t) - I_{sc}(t) \quad (29)$$

The current error is processed by the PI controller, whose output is expressed as

$$u_{sc}(t) = K_P e_{sc}(t) + k_i \int e_{sc}(t)\, dt \quad (30)$$

and its transfer function is

$$G_{PI}(s) = K_p + \frac{K_i}{8}. \quad (31)$$

The PI-controller output is applied to the PWM generator to produce the switching signals for Ssc1 and Ssc2. Thus, the SC current is regulated according to the required transient power.

During SC discharging, a sudden increase in DC-load power demand causes the supercapacitor to rapidly supply the required transient power to the DC bus. The power flow is

$$SC \rightarrow L_{sc} \rightarrow DC\ \ Bus$$

The SC power is given by

$$P_{sc} = V_{sc} I_{sc} \quad (32)$$

When the converter operates in boost mode, the ideal voltage relationship is

$$V_{dc} = \frac{V_{sc}}{1-D} \quad (33)$$

where D is the duty ratio. Hence,

$$D = 1 - \frac{V_{sc}}{V_{dc}} \quad (34)$$

When Ssc2 is ON and Ssc1 is OFF, the inductor stores energy from the supercapacitor. The inductor current is governed by

$$V_{L_{sc}} = L_{sc} \frac{dI_{L_{sc}}}{dt} \quad (35)$$

When Ssc2 is turned OFF, the stored energy in L_{sc} is transferred to the DC bus through the upper switching path. Consequently, the SC can respond rapidly to sudden load-power changes.

During SC charging, when excess PV power is available or the transient disturbance has disappeared, the direction of power flow is reversed:

$DC\ \ Bus \rightarrow L_{sc} \rightarrow SC$

The converter operates in buck mode, for which the ideal voltage relationship is

$$V_{sc} = DV_{dc} \qquad (36)$$

and therefore,

$$D = \frac{V_{sc}}{V_{dc}} \qquad (37)$$

The SC-side capacitor voltage is described by

$$I_{C_{sc}} = C_{sc}\frac{dV_{sc}}{dt} \qquad (38)$$

The approximate inductor-current ripple during boost operation is

$$\Delta IL_{sc} = \frac{V_{sc}D}{L_{sc}f_s} \qquad (39)$$

where fs denotes the converter switching frequency. A suitable Lsc reduces the current ripple and enables rapid but controlled power exchange.

The energy stored in the supercapacitor is

$$E_{sc} = \frac{1}{2}C_{sc}V_{sc}^2 \qquad (40)$$

which demonstrates its ability to rapidly absorb and release electrical energy. Unlike the BESS, the supercapacitor is therefore suited to high-power, short-duration disturbances.

VI. Single-Phase Grid Interface and Control Strategy

A. Single-Phase Grid-Connected VSC

The proposed hybrid energy system is connected to the single-phase utility grid through a bidirectional voltage source converter (VSC), as shown in Fig. 7. The VSC provides the electrical interface between the common dc bus and the utility grid and enables controlled bidirectional active-power exchange. The dc bus receives power from the photovoltaic (PV) source, battery energy storage system (BESS), and supercapacitor, while the VSC regulates the exchange of surplus or deficit power with the utility grid.

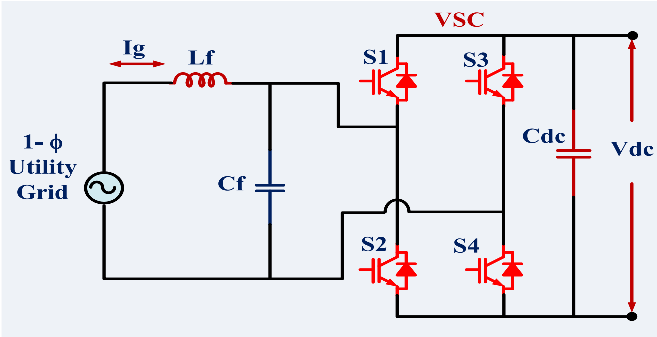

Fig.7 Single-Phase Utility Grid-Connected Voltage Source Converter (VSC)

The single-phase grid voltage is represented by

$$v_g(t) = V_{gm}\,sin(\theta_g) \qquad (41)$$

where V_{gm} is the peak grid voltage and θ_g is the instantaneous grid angle. The angular frequency is given by

$$\omega_g = \frac{d\theta_g}{dt} = 2\pi f_g \qquad (42)$$

For a 50-Hz utility system,

$$\omega_g = 314 \cdot 16ra\,d/s \qquad (43)$$

The VSC output is connected to the utility grid through an Lf–Cf filter. The filter inductance limits the current ripple produced by the switching operation, whereas the capacitor attenuates high-frequency switching components. The grid-current dynamics can be expressed as

$$L_f\frac{di_g}{dt} = v_{inv} - v_g - R_f i_g \qquad (44)$$

where v_{inv} is the converter-side voltage, i_g is the grid current, Lf is the filter inductance, and R_f is the equivalent filter resistance.

Equation (1) indicates that the grid current is controlled by regulating the voltage difference between the VSC and the utility grid. Therefore, the objective of the proposed controller is to generate an appropriate converter voltage reference such that the grid current follows its commanded reference with minimum steady-state error and reduced harmonic distortion.

B. Single-Phase Synchronous Reference Frame

Since the proposed interface is single-phase, direct application of conventional dq-axis transformation is not possible because a single-phase system does not inherently provide two orthogonal components as shown in Fig. 8. Hence, an artificial orthogonal component is generated from the measured grid voltage and current.

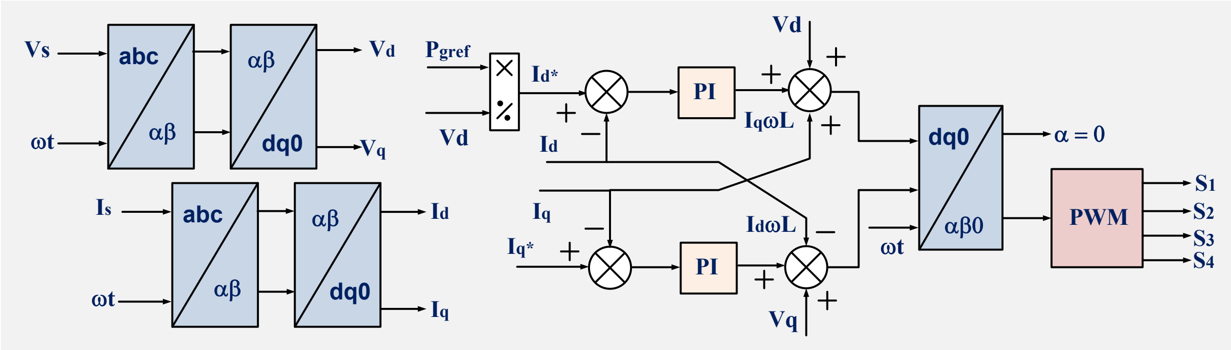

Fig.8 Single-Phase Grid-Connected VSC Control Strategy

The stationary reference-frame quantities are defined as

$v_\alpha = v_g, \qquad v_\beta = \hat{v}_g$

And

$i_\alpha = i_g, \qquad i_\beta = \hat{\imath}_g$

where $\hat{v}_g$ and $\hat{\imath}_g$ denote the corresponding virtual orthogonal components.

The αβ quantities are transformed into the synchronous reference frame using

$$v_d = v_\alpha \cos\theta + v_\beta \cos\theta \qquad (45)$$
$$v_q = -v_\alpha \sin\theta + v_\beta \cos\theta$$

And

$$i_d = i_\alpha \, a\cos\theta_g + i_\beta \sin\theta g \qquad (46)$$
$$i_q = -i_\alpha \sin\theta_g + i_\beta \cos\theta_g$$

The grid angle θg is obtained using a phase-locked loop (PLL). Under synchronized operation, the d-axis is aligned with the grid-voltage vector and consequently,

$v_q \to 0$

Therefore,

$v_d \to |V_g|$

This transformation converts the sinusoidal grid variables into quasi-dc quantities, allowing independent regulation of the active and reactive current components.

C. Active and Reactive Power Control

The instantaneous active and reactive powers in the synchronous reference frame are expressed as

$$Pg = v_d i_d + v_q i_q \qquad (47)$$
$$Q_g = v_q i_d - v_{d^1 q}$$

Consequently, the d-axis current directly controls the active power exchanged with the grid, whereas the q-axis current regulates reactive power.

The reference d-axis current is generated from the desired grid active power as

$$i_d^* = \frac{P_g^*}{v_d} \qquad (48)$$

where P_g^* is the commanded grid active power.

Similarly, the reactive-current reference is

$$i_q^* = -\frac{Q_g^*}{v_d} \qquad (49)$$

For unity-power-factor operation,

$$i_q^* = 0 \qquad (50)$$

Hence, the active-power exchange is controlled through id, while the reactive-power component is suppressed by forcing iq toward zero.

D. Decoupled dq-Axis Current Controller

The dq-axis model of the grid-side filter is obtained from (1) as

$$L_f \frac{di_d}{dt} = V_{inv,d} - V_d - R_f i_d + \omega_g L_f i_q \qquad (51)$$

And

$$L_f \frac{di_q}{dt} = V_{inv,q} - V_q - R_f i_q - \omega_g L_f i_d \qquad (52)$$

Equations (51) and (52) reveal the cross-coupling terms $\omega_g L_f i_d$

And

$-\omega_g L_f i_d$

These terms cause interaction between the active- and reactive-current control loops. To improve the dynamic response, the proposed controller incorporates cross-coupling compensation together with grid-voltage feedforward.

The current errors are defined as

$$e_d = i_d^* - i_d \qquad (53)$$
$$e_q = i_q^* - i_q$$

The PI controllers generate

$$u_d = K_{Pd} e_d + K_{id} \int e_d \, dt \qquad (54)$$
$$u_d = K_{pq} e_q + K_{iq} \int e_q \, dt \qquad (55)$$

The commanded converter voltages are then calculated as

$$v_{inv'd}^* = u_d + R_f i_d + u_d - \omega_g L_f i_q \qquad (56)$$
$$v_{inv,q}^* = v_q + R_f i_q + u_q + \omega_g L_f i_{d.} \qquad (57)$$

The grid-voltage terms in (56) and (57) provide feedforward compensation, whereas the ωgLf terms compensate for the cross coupling between the two synchronous axes. Therefore, the d- and q-axis current dynamics are approximately decoupled, enabling independent active- and reactive-power regulation.

E. Voltage Reference Generation and PWM

After current regulation, the commanded converter voltages are transformed from the synchronous reference frame to the stationary reference frame using the inverse Park transformation:

$$v_{\alpha}^{*} = v_{inv,d}^{*} \cos\theta_g - v_{inv,q}^{*} \sin\theta_g \qquad (58)$$

$$v_{\beta}^{*} = v_{inv,d}^{*} \sin\theta_g + v_{inv,q}^{*} \sin\theta_g \qquad (59)$$

The resulting modulation reference is applied to the PWM generator to produce the gating signals

S1, S2, S3, S4.

These switching signals determine the instantaneous converter voltage and consequently regulate the grid current according to the commanded power reference.

F. DC-Bus and Grid Power Coordination

The grid-side controller is coordinated with the dc-side energy sources through the dc-bus power balance,

$$P_{PV} + P_B + P_{SC} = P_L + P_g + P_{loss} \qquad (60)$$

where PPV, PB, and PSC represent the PV, battery, and supercapacitor powers, respectively; PL represents the local dc-load power; Pg represents grid power; and Ploss represents converter and filter losses.

Accordingly, the grid power reference can be expressed as

$$P_g^{*} = P_{PV} + P_B + P_{SC} - P_L - P_{loss} \qquad (61)$$

This establishes a direct relationship between renewable-energy availability and grid power exchange. During excess renewable generation, the VSC can transfer surplus power to the utility grid, whereas during a power deficit, the grid can supply the required energy. The battery and supercapacitor provide additional dynamic support to maintain dc-bus power balance.

VII. LINEAR ACTIVE DISTURBANCE REJECTION CONTROL

Linear Active Disturbance Rejection Control (LADRC) is a control approach designed to mitigate the effects of external disturbances, parameter uncertainties, and system nonlinearities by actively estimating and compensating these disturbances in real time. The LADRC employs a Linear Extended State Observer (LESO) to estimate the system states and lumped disturbance, thereby improving the robustness of the controlled system. The control structure of the proposed LADRC is shown in Fig. 9.

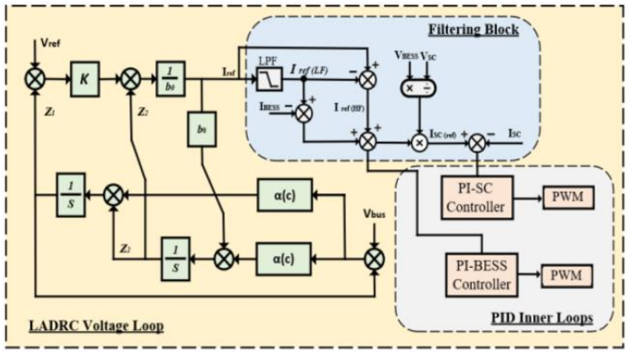

Fig. 9. LADRC-based HESS control scheme architecture.

To analyze the system dynamics, consider a general first-order system described by

$$\dot{y} = -a_0 y + w + bu \qquad (62)$$

where y and u denote the system output and control input, respectively, w represents an unknown external disturbance, a0 is the known system parameter, and b denotes the actual control gain, which may be uncertain. To accommodate the uncertainty associated with b, an estimated control gain b0 is introduced. By adding and subtracting b0u, (17) can be rewritten as

$$\dot{y} = b_0 u + f(y, w) \qquad (63)$$

where the generalized disturbance is defined as

$$f(y, w) = -a_0 y + w + (b - b_0)u \qquad (64)$$

Thus, the system dynamics can be expressed in the state-space form as

$$\begin{bmatrix} \dot{x}_1 \\ \dot{x}_2 \end{bmatrix} = \begin{bmatrix} 0 & 1 \\ o & 0 \end{bmatrix} \begin{bmatrix} x_1 \\ x_2 \end{bmatrix} + \begin{bmatrix} 0 \\ b_0 \end{bmatrix} u + \begin{bmatrix} 0 \\ 1 \end{bmatrix} f \qquad (65)$$

where x1=y and x2=y˙. The term f represents the generalized disturbance and incorporates the effects of external disturbances, system uncertainties, and control-gain mismatch.

The LESO is designed to estimate both the system state and the generalized disturbance f. The observer is formulated as

$$\begin{pmatrix} \dot{z}_1 \\ \dot{z}_2 \end{pmatrix} = \begin{bmatrix} \beta_1 & 1 \\ -\beta_2 & 0 \end{bmatrix} \begin{bmatrix} 21 \\ z_2 \end{bmatrix} + \begin{bmatrix} \beta_1 & 1 \\ -\beta_2 & 0 \end{bmatrix} \begin{bmatrix} u \\ y \end{bmatrix} \qquad (66)$$

where z1 estimates the system output y, while z2 estimates the generalized disturbance f. The observer gains β1 and β2 determine the convergence speed and estimation accuracy of the LESO.

Using the estimated disturbance z_2, the control input is formulated as

$$u = \frac{-z_2 + u_0}{b_0} \qquad (67)$$

where u0 is the auxiliary control variable responsible for reference tracking. Substituting (20) into the system model gives

$$\dot{y} = f + b_0\left(\frac{-z_2+u_0}{b_0}\right) \quad (68)$$

When the estimated disturbance converges to the actual generalized disturbance,

$z_2 \to f$

the system dynamics reduce to

$\dot{y} = u_0$

Thus, LADRC effectively transforms the uncertain plant into a controllable integrator by actively compensating the generalized disturbance.

The auxiliary control variable is defined as

$$u_0 = K_{LADRC}\left(V_{ref} - z_1\right) \quad (69)$$

where V_{ref} denotes the reference value and KLADRC is the proportional control gain. Accordingly, the closed-loop transfer function of the LADRC-controlled system is obtained as

$$\phi(s) = \frac{K_{LADRC}}{s+K_{LADRC}} \quad (70)$$

which represents a first-order closed-loop response. The corresponding closed-loop pole is located at

$s = -K_{LADRC}$

indicating stable operation for

$K_{LADRC} > 0$

This formulation demonstrates the principal advantage of LADRC, wherein the effects of disturbances and parameter uncertainties are estimated through the LESO and compensated directly through the control input, thereby improving the disturbance rejection and reference tracking capability of the controlled system.

VII. Simulation Results and Discussion

The proposed PV-BESS-SC system is evaluated in MATLAB/Simulink under variable load conditions. The performance is compared for two configurations: without supercapacitor (SC) and with SC. The dc-link voltage, battery current, load current, PV current, PV power, and grid power are analyzed to demonstrate the transient-support capability of the SC.

A. DC-Link Voltage Response

Fig. 10 shows the dc-link voltage response. The voltage rapidly rises from 0 V during initialization and reaches the reference value of approximately 400 V. Without the SC, significant oscillations are observed during the initial transient and load transitions, with the peak voltage reaching approximately 440–450 V. With the SC, the transient oscillations are considerably reduced and the voltage remains close to 400 V. The enlarged waveform indicates that the SC effectively compensates the short-duration power imbalance at the dc bus. Thus, the SC improves dc-link voltage regulation by supplying or absorbing transient power.

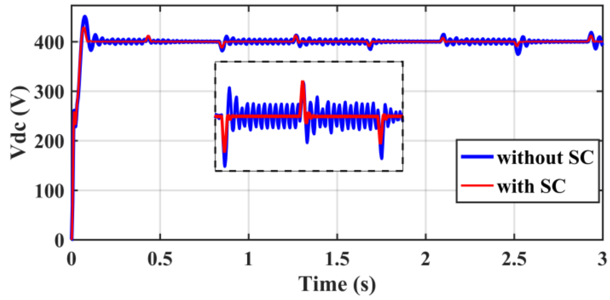

Fig. 10. DC-link voltage response with and without supercapacitor.

B. Battery Current Response

Fig. 11 presents the battery-current response. The battery current exhibits transient peaks of approximately ±35–38 A during the initial operating condition. Under the subsequent load transitions, the battery current varies approximately between −5 and +15 A, depending on the charging or discharging condition. Without the SC, considerable high-frequency oscillations are superimposed on the battery current. With the SC, these oscillations are substantially attenuated, while the average battery current remains nearly unchanged. This indicates that the SC supplies the high-frequency power component and allows the battery to handle the relatively slower energy component.

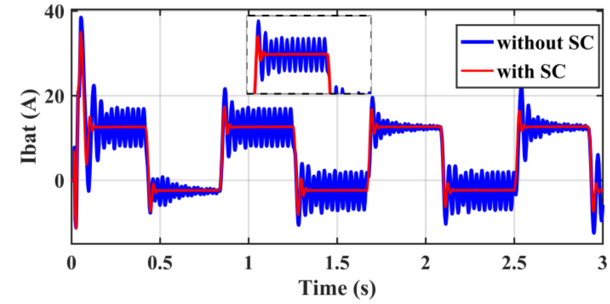

Fig. 11. Battery current response under variable load conditions.

C. Load Current Response

The load-current waveform is shown in Fig. 12. The load changes between approximately 5 A and 15 A, with transitions occurring at approximately 0.5, 1.0, 1.5, 2.0, and 2.5s. Both configurations successfully track the commanded load current. The response with the SC exhibits reduced transient oscillations during the switching intervals, while the steady-state current remains approximately 5 A or 15 A according to the applied load condition. Therefore, the integration of the SC does not affect the required load-current regulation.

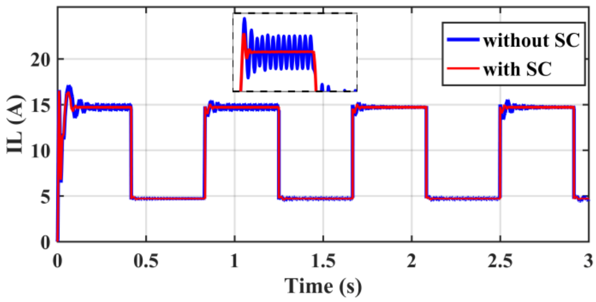

Fig. 12. Load current response under variable operating conditions.

D. PV Current Response

Fig. 13 shows the PV current response. After the initial transient, the PV current settles at approximately 26 A. During the initial condition, the current reaches nearly 45–48 A before settling to its steady-state operating value. The system without the SC exhibits comparatively higher oscillations, particularly around 1.0–1.5 s. With the SC, these fluctuations are reduced and the PV current remains close to 26 A. This confirms that the SC absorbs rapid power variations without significantly modifying the steady-state PV operating point.

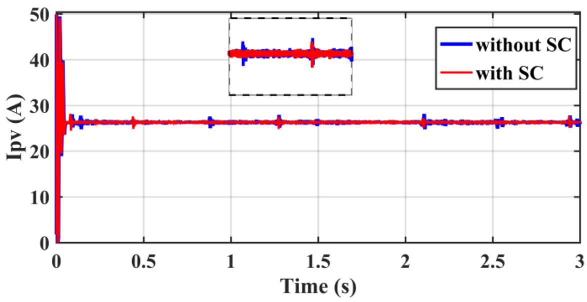

Fig. 13. Photovoltaic source current response.

E. PV Power Response

The PV power response is presented in Fig. 14. Following the initial transient, the PV system supplies approximately 4.4–4.6 kW under steady-state operation. The initial transient produces a peak of approximately 5 kW. During the interval around 1.0–1.5 s, the configuration without the SC exhibits considerable power oscillations, reaching approximately 6–6.5 kW in the enlarged region. The SC-assisted configuration produces a considerably smoother response. Hence, the SC improves the transient power balance while maintaining approximately the same steady-state PV power.

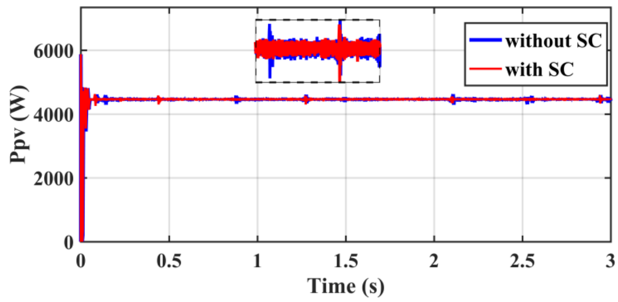

Fig. 14. Photovoltaic power response under transient operating conditions.

F. Grid Power Response

Fig. 15 presents the grid-power response. The grid initially experiences a transient power variation and subsequently settles at approximately 1.7–1.8 kW. During the transient interval around 1.0–1.5 s, the system without the SC exhibits considerably larger power fluctuations, whereas the SC-assisted system maintains a smoother response around the required power level. The grid power is governed by

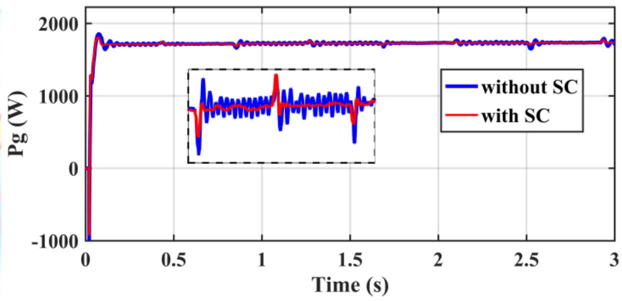

Fig. 15. Utility grid power response under variable load conditions.

The additional PSC term allows the supercapacitor to compensate rapid power mismatches, thereby reducing the power fluctuations transferred to the utility grid.

G. Hybrid Energy Storage Current Dynamics

Fig. 16 presents the coordinated current response of the PV source, battery, load, and supercapacitor. The PV current remains nearly constant at 26–27 A, whereas the load current changes between 5 and 15 A at the applied load transitions. The battery current follows the average load requirement, reaching approximately 12–13 A during the high-load intervals. In contrast, the supercapacitor current remains close to zero during steady-state operation and responds primarily during transient events. This indicates that the SC provides rapid power compensation, while the battery handles the sustained energy demand. Hence, the hybrid storage arrangement achieves effective current sharing and limits high-frequency variations in the battery current.

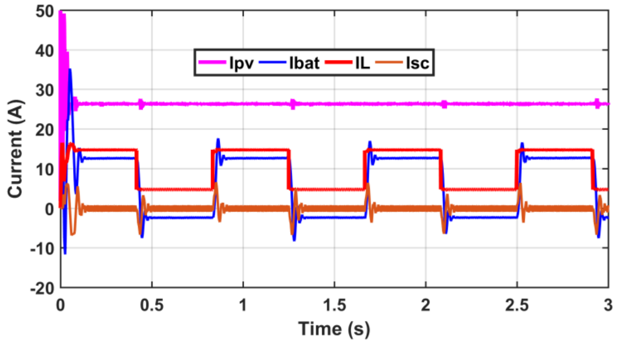

Fig. 16. Current-sharing characteristics of the PV-BESS-SC system.

H. Power-Sharing Performance of the Hybrid Energy Storage System

Fig. 17 shows the power-sharing characteristics of the proposed PV-BESS-SC system under variable load conditions. The PV power PPV remains nearly constant at 4.5 kW, while the load power PL alternates between approximately 2 and 6 kW. During high-load operation, the battery supplies approximately 3.3–3.5 kW, whereas its power contribution decreases during the low-load interval. The supercapacitor power PSC remains close to zero during steady-state operation but responds rapidly during load transitions, reaching transient values of approximately ±2 kW. The grid power Pg remains around 1.7–1.8 kW, providing the remaining power required by the system. Thus, the SC effectively compensates short-duration power mismatches, while the battery and grid provide the sustained energy demand.

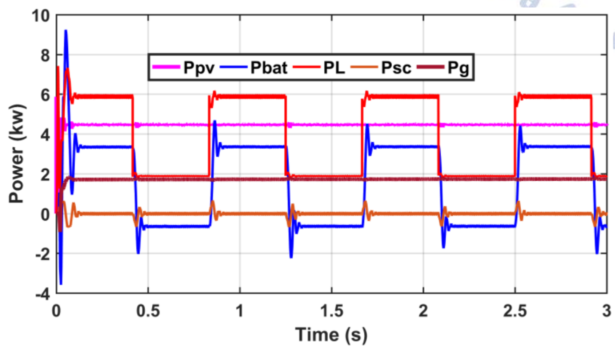

Fig. 17. Power-sharing characteristics of the PV-BESS-SC system.

I. Grid Voltage and Current Response

Fig. 18 presents the utility-grid voltage Vg and grid current Ig. The grid voltage exhibits a sinusoidal waveform with an approximately 230 V peak magnitude, corresponding to about 162 V rms. The voltage remains periodic throughout the 3 s simulation, confirming stable grid synchronization. The grid current remains sinusoidal and approximately centered around zero, with a steady-state peak of about 15–16 A. During the transient interval highlighted in the inset, the current reaches approximately 30–48 A before settling to its normal operating range. The close tracking of the grid current with the grid voltage demonstrates proper VSC synchronization and controlled power exchange with the utility grid.

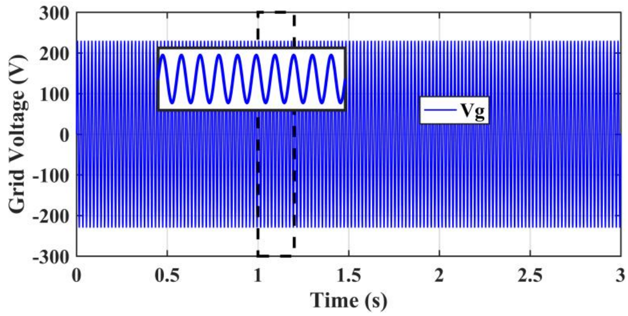

(a)

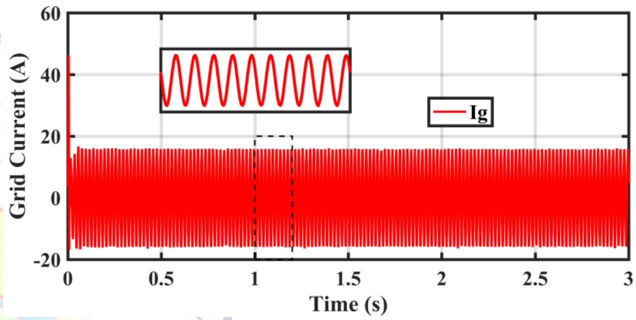

(b)

Fig. 18. Single-phase utility grid (a) voltage, (b) current responses.

IX. Grid Current THD Analysis

The grid-current harmonic spectra show a reduction in total harmonic distortion (THD) with the integration of the supercapacitor. Without the SC, the grid-current THD is 2.59%, whereas with the SC, the THD decreases to 1.64%.

The corresponding THD reduction is

$\Delta THD = 2.59 - 1.64 = 0.95\%$

and the percentage reduction is

$\frac{2.59-1.64}{2.59} \times 100 = 36.68\%$

Thus, the proposed SC integration achieves a 36.68% reduction in grid-current THD, demonstrating improved grid-side power quality.

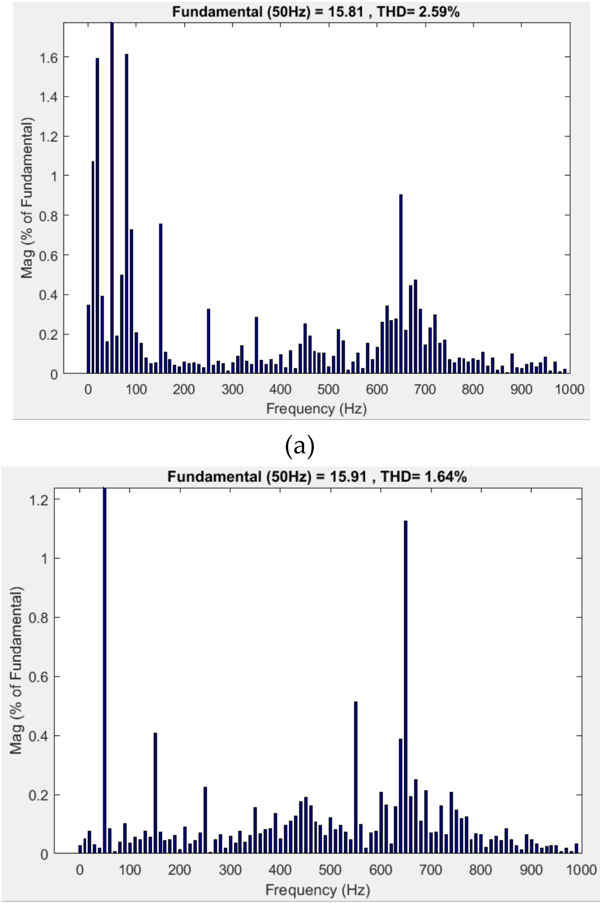

(a)

(b)

Fig. 19 Grid Current THD Comparison (a) Without and (b) With Supercapacitor

X. Conclusion

This paper presented a hybrid PV-BESS-supercapacitor system with coordinated energy management and grid-interfaced control for enhanced dynamic performance and power quality. The proposed configuration integrates the PV source, battery energy storage system, and supercapacitor through a common dc bus to achieve effective power sharing under varying operating conditions. The simulation results demonstrate that the battery primarily supplies the average power demand, whereas the supercapacitor provides rapid transient power compensation. This complementary operation reduces battery-current fluctuations and improves the dynamic regulation of the dc-link voltage. The proposed control strategy also enables effective coordination between renewable generation, energy storage, load demand, and utility-grid power exchange. The grid-current harmonic analysis further confirms the effectiveness of the proposed configuration. The integration of the supercapacitor significantly reduces harmonic distortion in the grid current, thereby improving the overall power quality of the grid interface. The improved transient response and smoother power exchange demonstrate the capability of the hybrid energy storage system to handle rapid variations in power demand. The proposed PV-BESS-supercapacitor configuration provides improved power sharing, enhanced dc-link voltage stability, reduced battery stress, and better grid-current quality. The developed system therefore offers a suitable approach for reliable and power-quality-oriented renewable-energy-based grid-interactive applications.

Conflict of interest statement

Authors declare that they do not have any conflict of interest.

References

[1] S. Tan et al., “Lyapunov-based resilient cooperative control for DC microgrid clusters against false data injection cyber-attacks,” IEEE Trans. Smart Grid, vol. 15, no. 3, pp. 3208–3222, May 2024.

[2] A. Aghmadi, H. Hussein, K. H. Polara, and O. Mohammed, “A comprehensive review of architecture, communication, and cybersecurity in networked microgrid systems,” Inventions, vol. 8, no. 4, p. 84, Jun. 2023.

[3] L. Wang et al., “Grid resilience enhancement and stability improvement of an autonomous DC microgrid using a supercapacitor-based energy storage system,” IEEE Trans. Ind. Appl., vol. 60, no. 2, pp. 1975–1985, Mar./Apr. 2024.

[4] Y. Zeng et al., “Fixed-time secondary controller for rapid state-of-charge balancing and flexible bus voltage regulation in DC microgrids,” IEEE Trans. Power Syst., vol. 39, no. 3, pp. 5393–5407, May 2024.

[5] K. A. Khan and M. Khalid, “Improving the transient response of hybrid energy storage system for voltage stability in DC microgrids using an autonomous control strategy,” IEEE Access, vol. 9, pp. 10460–10472, 2021.

[6] W. Jing, C. H. Lai, S. H. W. Wong, and M. L. D. Wong, “Battery-supercapacitor hybrid energy storage system in standalone DC microgrids: A review,” IET Renew. Power Generation, vol. 11, no. 4, pp. 461–469, Mar. 2017.

[7] S.-J. Ahn, J.-W. Park, I.-Y. Chung, S.-I. Moon, S.-H. Kang, and S.-R. Nam, “Power-sharing method of multiple distributed generators considering control modes and configurations of a microgrid,” IEEE Trans. Power Del., vol. 25, no. 3, pp. 2007–2016, Jul. 2010.

[8] A. G. Olabi, C. Onumaegbu, T. Wilberforce, M. Ramadan, M. A. Abdelkareem, and A. H. Al–Alami, “Critical review of energy storage systems,” Energy, vol. 214, Jan. 2021, Art. no. 118987.

[9] A. Etxeberria, I. Vechiu, H. Camblong, and J. M. Vinassa, “Hybrid energy storage systems for renewable energy sources integration in microgrids: A review,” in Proc. Conf. IPEC, 2010, pp. 532–537, Accessed: Nov. 25, 2023. [Online]. Available: https://ieeexplore.ieee.org/abstract/document/5697053/

[10] A. Aghmadi and O. A. Mohammed, "Energy storage systems: Technologies and high-power applications," Batteries, vol. 10, no. 4, p. 141, Apr. 2024.

[11] T. Bocklisch, "Hybrid energy storage systems for renewable energy applications," Energy Procedia, vol. 73, pp. 103–111, Jun. 2015.

[12] X. Chang, Y. Li, X. Li, and X. Chen, "An active damping method based on a supercapacitor energy storage system to overcome the destabilizing effect of instantaneous constant power loads in DC microgrids," IEEE Trans. Energy Convers., vol. 32, no. 1, pp. 36–47, Mar. 2017.

[13] W. Jiang, Z. Wang, J. Wang, X. Zhang, and P. Wang, "Decentralized autonomous energy management strategy for multi-paralleled hybrid energy storage systems in the DC microgrid with mismatched line impedance," IEEE Trans. Sustain. Energy, vol. 15, no. 2, pp. 1114–1126, Apr. 2024.

[14] G. Oriti, A. L. Julian, M. P. Storm, D. P. Detoma, and N. Anglani, "Shipboard control system supported by energy storage sizing to meet the MIL-STD-1399 limits for pulsed power loads," IEEE Open J. Ind. Appl., vol. 4, pp. 279–290, Aug. 2023.

[15] W.-S. Im, C. Wang, L. Tan, W. Liu, and L. Liu, "Cooperative controls for pulsed power load accommodation in a shipboard power system," IEEE Trans. Power Syst., vol. 31, no. 6, pp. 5181–5189, Nov. 2016.

[16] M. Farhadi, A. Mazloomzadeh, and O. Mohammed, "Comparative analysis of energy control techniques for DC microgrid and pulsed power load applications," in Proc. 40th Annu. Conf. IEEE Ind. Electron. Soc., Feb. 2014, pp. 4204–4210.

[17] J. Fang, Y. Tang, H. Li, and X. Li, "A battery/ultracapacitor hybrid energy storage system for implementing the power management of virtual synchronous generators," IEEE Trans. Power Electron., vol. 33, no. 4, pp. 2820–2824, Apr. 2018.

[18] J. Hou, J. Sun, and H. Hofmann, "Battery/flywheel Hybrid Energy Storage to mitigate load fluctuations in electric ship propulsion systems," in Proc. Amer. Control Conf., Jun. 2017, pp. 1296–1301.

[19] H. S. Salama, K. M. Kotb, I. Vokony, and A. Dán, "The role of hybrid battery—SMES energy storage in enriching the permanence of PV— wind DC microgrids: A case study," Eng, vol. 3, no. 2, pp. 207–223, Mar. 2022.

[20] J. Li, M. Zhang, Q. Yang, Z. Zhang, and W. Yuan, "SMES/battery hybrid energy storage system for electric buses," IEEE Trans. Appl. Supercond., vol. 26, no. 4, pp. 1–5, Jun. 2016.

[21] K. C. Omran and A. Mosallanejad, "SMES/battery hybrid energy storage system based on bidirectional Z-source inverter for electric vehicles," IET Electr. Syst. Transp., vol. 8, no. 4, pp. 215–220, Dec. 2018.

[22] Z. Zheng et al., "Dual model predictive controlled hybrid energy storage system for naval DC microgrids," IEEE Trans. Transp. Electrif., vol. 9, no. 1, pp. 156–168, Mar. 2023.

[23] M. K. Behera and L. C. Saikia, "A novel resilient control of grid-integrated solar PV-hybrid energy storage microgrid for power smoothing and pulse power load accommodation," IEEE Trans. Power Electron., vol. 38, no. 3, pp. 3965–3980, Mar. 2023.

[24] L. Deng, G. Zhou, Y. Li, and Z. Chen, "Communication-free pulsed power distribution and tracking method for hybrid energy storage system based on active disturbance rejection control," IEEE Trans. Power Electron., vol. 39, no. 3, pp. 3024–3036, Mar. 2024.

[25] P. K. Behera and M. Pattnaik, "Coordinated power management of a laboratory scale wind energy assisted LVDC microgrid with hybrid energy storage system," IEEE Trans. Consum. Electron., vol. 69, no. 3, pp. 467–477, Aug. 2023.

[26] P. Gao, Y. Li, W. Yao, X. Zheng, and C. Zhang, "Optimization of hybrid energy storage system sizing with considering energy management strategy for high-power pulsed load in aircraft," IEEE Trans. Veh. Technol., vol. 72, no. 4, pp. 4525–4537, Apr. 2023.

[27] M. S. Wasim, S. Habib, M. Amjad, A. R. Bhatti, E. M. Ahmed, and M. A. Qureshi, "Battery-ultracapacitor hybrid energy storage system to increase battery life under pulse loads," IEEE Access, vol. 10, pp. 62173–62182, 2022.

[28] T. K. Roy, M. A. Mahmud, A. M. T. Oo, M. E. Haque, K. M. Muttaqi, and N. Mendis, "Nonlinear adaptive backstepping controller design for islanded DC microgrids," IEEE Trans. Ind. Appl., vol. 54, no. 3, pp. 2857–2873, May/Jun. 2018.

[29] M. Li, L. Wang, Y. Wang, and Z. Chen, "Sizing optimization and energy management strategy for hybrid energy storage system using multiobjective optimization and random forests," IEEE Trans. Power Electron., vol. 36, no. 10, pp. 11421–11430, Oct. 2021.

[30] X. Lu and H. Wang, "Optimal sizing and energy management for cost-effective PEV hybrid energy storage systems," IEEE Trans. Ind. Informat., vol. 16, no. 5, pp. 3407–3416, May 2020.